

Complexities in STEM analyses of polymer blend thin films

K. E. SICKAFUS, S. D. BERGER, A. M. DONALD

University of Cambridge, Cavendish Laboratory, Cambridge CB3 0HE, UK

Polystyrene (PS)-polyether sulphone (PES) polymer blend thin films were prepared for examination in a scanning transmission electron microscope. The microstructures observed in 75 wt% PS-25 wt% PES films consisted of spherical inclusions, ranging from ~ 0.2 to $\sim 1.2 \mu\text{m}$ in diameter. X-ray spectrometric analysis in the microscope revealed that the inclusions were PES-rich, while the matrix contained only PS. Attention in this paper is paid to the contrast in the annular dark-field detector (ADF) images from these thin films. This image contrast has a complicated dependence on both the angular range subtended by the dark-field detector and "mass-thickness" variations within the films. On microscopes with appropriate lens controls which permit the acceptance angle of the ADF detector to be varied, it becomes possible actually to reverse the contrast between the two phases.

1. Introduction

The study of polymeric materials using electron microscopy (EM) is difficult due to the susceptibility of polymers to radiation damage. However, some polymers are fairly resistant to electron beam damage and structural analyses of such materials have been achieved using EM (e.g. "craze" structures in polystyrene [1]). Recently, compositional analyses of polymers have been carried out using scanning electron microscopy (SEM) [2], and scanning transmission electron microscopy (STEM) [3]. Composition is usually determined from spectroscopic analysis, but recent work on non-polymeric materials has demonstrated that image analysis may be used to provide chemical information in certain circumstances [4], and this has advantages for beam-sensitive materials. Image analysis is a high-signal technique and the signal can be collected rapidly. Spectroscopy, on the other hand, is low-signal and requires a long accumulation time, and hence is not as useful for specimens susceptible to radiation damage.

In the study presented here, a dedicated STEM was used to characterize the microstructures present in thin films of the polymer blend polystyrene (PS)-polyether sulphone (PES). Initially, information on the local atomic composition was obtained using an energy-dispersive X-ray spectrometer. In addition, the contrast observed in annular dark-field STEM images from these specimens was analysed, to examine the effectiveness of image analysis compared with spectroscopy. Dark-field STEM contrast from these films was complicated due to multiple scattering, as will be illustrated.

2. Experimental procedure

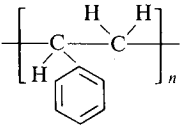
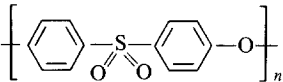
Thin films of PS-PES polymer blends were cast from solution following dissolution of the pure components in the co-solvent cyclohexanone. The PS ($M_n = 109\,500$) was obtained from Polymer

Laboratories Ltd. The PES ($M_n = 18\,000$) was provided by Imperial Chemicals Industries plc. The cyclohexanone solvent was 99.8% purity research grade and was obtained from Aldrich Chemicals Co. Ltd. The structural unit of each polymer component and other statistics are listed in Table I. The polymer-solvent solution was diluted to ~ 3 wt% polymer and contained three parts PS to one part PES by weight.

The polymer blend thin films were produced by immersing a glass slide in the solution, and withdrawing it at a constant draw rate of 1 mm s^{-1} . The solution was maintained at a temperature between 30 and 40°C during drawing. Each film was then removed from its glass slide substrate for examination in the STEM, by floating the polymer film off on a distilled-water bath and lifting a small portion of the film on to a 3 mm copper grid. The film on the copper grid was examined using either a VG HB-5 dedicated STEM operating at 80 kV, a VG HB-501 dedicated STEM operating at 100 kV, or a Philips 400T TEM/STEM operating at 100 kV. The VG STEMs both employ a field emission source, while the Philips 400T was operated with a standard tungsten filament. Conventional electron diffraction measurements revealed that all the specimens were in the amorphous state.

The films produced by the procedure described above were rather thick. Measurements using a Talysurf 4 profilometer indicated that the particular PS-PES specimen discussed in detail here was $\sim 410 \text{ nm}$ thick. With much higher spatial resolution, the thicknesses of the microstructural features in the same film were estimated using electron energy-loss spectrometry (EELS), by analysing EELS spectra obtained using a VG spectrometer on the HB-501 STEM. The thickness estimated from such spectra were determined either by ratioing the intensity in the first plasmon loss peak to the intensity in the zero-loss peak [5], or by ratioing the loss energy of maximum intensity to the first plasmon energy (when the intensity

TABLE I Polystyrene and polyether sulphone

Property	Polymer	
	Polystyrene (PS)	Polyether sulphone (PES)
Monomer unit		
Material	PS standard from Polymer Laboratories, Ltd	General purpose grade PES 4100P from Imperial Chemical Industries
Monomer mol. wt. (a.m.u.)	104	232
Number mol. wt.	109, 500 ($M_w/M_n < 1.05$)	18 000 ($M_w/M_n > 2$)
Monomers per chain (av.)	1050	78
Density (kg m^{-3})	$1.04 \text{ to } 1.06 \times 10^3$	1.37×10^3
Monomer volume (m^3)	1.64×10^{-28}	2.81×10^{-28}
Glass transition ($^\circ\text{C}$)	~ 100	~ 222

in the first plasmon loss could not be estimated accurately). Either of these ratios is proportional to t/Λ_p , where t is the film thickness and Λ_p is the mean free path for the plasmon loss event. $\Lambda_p(\text{PS})$ and $\Lambda_p(\text{PES})$ were not measured, but in EELS spectra from both polymers a first plasmon peak was observed at $\sim 24 \text{ eV}$, which is the first plasmon loss for carbon [6]. Thus $\Lambda_p(\text{PS})$ and $\Lambda_p(\text{PES})$ were taken to be approximately equal to $\Lambda_p(\text{C})$. Using the Ferrel equation [7], it was determined that $\Lambda_p(\text{C}) \sim 91 \text{ nm}$ for 100keV electrons. So for thickness determinations from the EELS spectra which appear later, it was assumed that $\Lambda_p(\text{PS}) = \Lambda_p(\text{PES}) = \Lambda_p(\text{C}) = 91 \text{ nm}$.

The microanalytical facility used was a Link Systems 860, with an energy-dispersive X-ray spectrometer (EDS) attached to the HB-5 STEM. This system allows one to select an energy window containing a particular fluorescence X-ray peak, and then to map the X-ray intensity digitally, in the form of a 128×128 pixel array. The X-ray intensity at each pixel in a map was represented on a 16-level grey scale, with a black pixel representing 0 X-ray counts, and a white pixel representing 15 X-ray counts. The map presented here represents cumulative data from 15 repeated scans of a selected specimen area, with an electron beam dwell-time of 2 msec. The X-ray spectrometer is separated from the microscope vacuum by a thin beryllium window, limiting the detection of elements to those with atomic number $Z > 11$. Thus, for the polymer blend discussed here, the interest is in the detection of sulphur ($Z = 16$), only present in the PES component. In performing the EDS analyses of these specimens, the sulphur fluorescence X-ray peak, $SK\alpha$, was monitored to provide information on the local PES content of the various microstructural features. Thus, the presence of the PS component in these PS-PES blend thin films could only be inferred from a lack of $SK\alpha$ signal at certain locations within the microstructure.

The principle electron-imaging techniques employed in this STEM study were annular dark-field (ADF) imaging and bright-field (BF) imaging. The electron

detection arrangement for ADF and BF imaging in a STEM are illustrated schematically in Fig. 1. The image interpretation procedures employed will be described in the next section.

3. Results and discussion

3.1. Microanalytical results

3.1.1. PS-PES microstructures

Fig. 2 shows STEM observations of the microstructures present in a typical PS-PES polymer blend thin films. The films exhibited a microstructure consisting of spherical inclusions (as seen in projection). Fig. 2 shows that inclusions ranging in size from ~ 0.2 to $\sim 1.2 \mu\text{m}$ diameter were observed. The range of sizes was not continuous, but rather contained two distinct size distributions, one centred at $\sim 0.3 \mu\text{m}$ and the other $\sim 0.7 \mu\text{m}$ diameter.

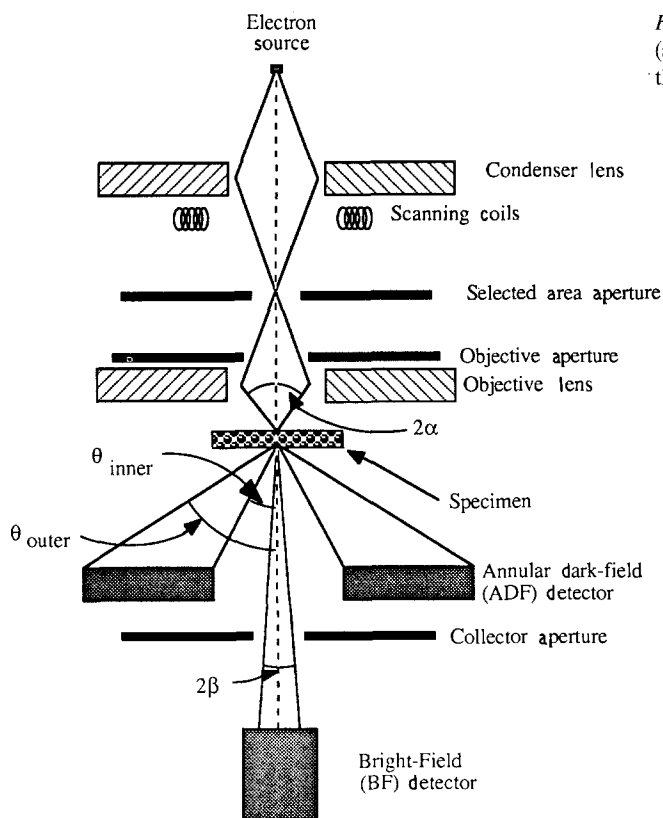
3.1.2. PS-PES X-ray data

Information concerning the compositions of the inclusions and the surrounding matrices in each film was obtained from digital X-ray maps of the $SK\alpha$ signal from selected regions of each specimen. Fig. 2c shows an $SK\alpha$ X-ray map from a PS-PES polymer blend thin film. It is a $3 \mu\text{m} \times 3 \mu\text{m}$ map of the region shown in Figs 2a and b. Recalling that white pixels in the map represent sulphur-rich regions, and black pixels represent sulphur-deficient regions, it is evident from Fig. 2c that the inclusions are sulphur-rich compared with the matrix material. Thus, the inclusions in this film appear to be PES-rich, and by inference, the matrix must be PS-rich due to its lack of sulphur.

3.1.3. PS-PES electron images

Figs 2a and b show BF and corresponding ADF images of the microstructure in the PS-PES polymer blend thin film, obtained using the HB-5 STEM. Figs 2d and e are an analogous BF/ADF image pair from the same film, obtained using the HB-501 STEM. The two BF images exhibit similar contrast: the inclusions are dark, the matrix material is light. On the other hand, the ADF images from the two

Figure 1 Schematic diagram of the arrangement in a typical STEM (single condenser lens) and electron ray paths, for electrons leaving the source and arriving at either the BF or ADF detector.



instruments exhibit different contrast. In the ADF image from the HB-5 (Fig. 2a) the spherical inclusions are dark, whereas in the ADF image from the HB-501 (Fig. 2e) the spheres are bright. As shown above, X-ray data show that the inclusions are PES-rich (i.e. have higher average Z), while the matrix is PES-deficient. One would therefore naively expect the ADF image *always* to show bright spheres. It will be shown below that the difference in contrast can be ascribed to multiple scattering and the different ranges of angular acceptance of the dark-field detectors on the two microscopes.

Fig. 3 shows ADF observations of the microstructure present in a representative area of this same PS-PES film, using all three STEM instruments described in the experimental procedure (the same area is imaged in each micrograph of Fig. 3). The various angular ranges of scattering accepted by the ADF detectors in the different microscopes lead to contrast differences as before. For example, the PES-rich inclusions again appear bright relative to the matrix in the HB-501 (Fig. 3b), but dark relative to the matrix in HB-5 (Fig. 3a). The results using the Philips 400T show a similar effect: at low angles (camera length $L = 575$ mm, Fig. 2c) the ADF detector receives more electrons from the PS than the PES inclusions, but at high angles (camera length $L = 290$ mm, Fig. 2e) more electrons are received from the PES. At intermediate angles (camera length $L = 400$ mm) contrast is essentially zero. The angular regimes on the Philips 400T may be compared directly with that on the HB-501 since the same 100 keV operating voltage was used on these instruments. (Note: the Philips beam convergence angle $2\alpha \leq 15$ mrad (see Fig. 1); hence, overlap between the

transmitted convergent-beam disc and the ADF detector at all camera lengths used here was avoided. However, such a small C_2 aperture resulted in low image intensity; thus the spatial resolution in these images is limited due to shot noise.)

3.2. Image interpretation

Fig. 2 contains both BF and ADF images of these polymer blend thin films. This section attempts to analyse the contrast observed in these images. The objective of this exercise is to determine if information on PS-PES microstructural composition can be obtained from ADF images, as an alternative to the (high beam-exposure) EDS analysis.

3.2.1. Theory

In a STEM, an image is formed by scanning a focused electron beam across the specimen and detecting the transmitted current. The various imaging possibilities arise from using discriminating schemes that select only portions of the transmitted current. To produce an ADF image, the current reaching an annular detector at the beam exit side of the specimen (Fig. 1) is monitored, while a BF image is produced by collecting a small cone of angles defined by the collector aperture (see Fig. 1). For a general discussion of STEM, see Brown [8].

3.2.1.1. Bright-field detector. This detector collects a small solid-angular range about the optic axis, as defined by the collector aperture. The collected current consists of those electrons that are unscattered or elastically scattered through small angles, plus electrons that are inelastically scattered. The contrast observed in a BF image is complicated due to coherency

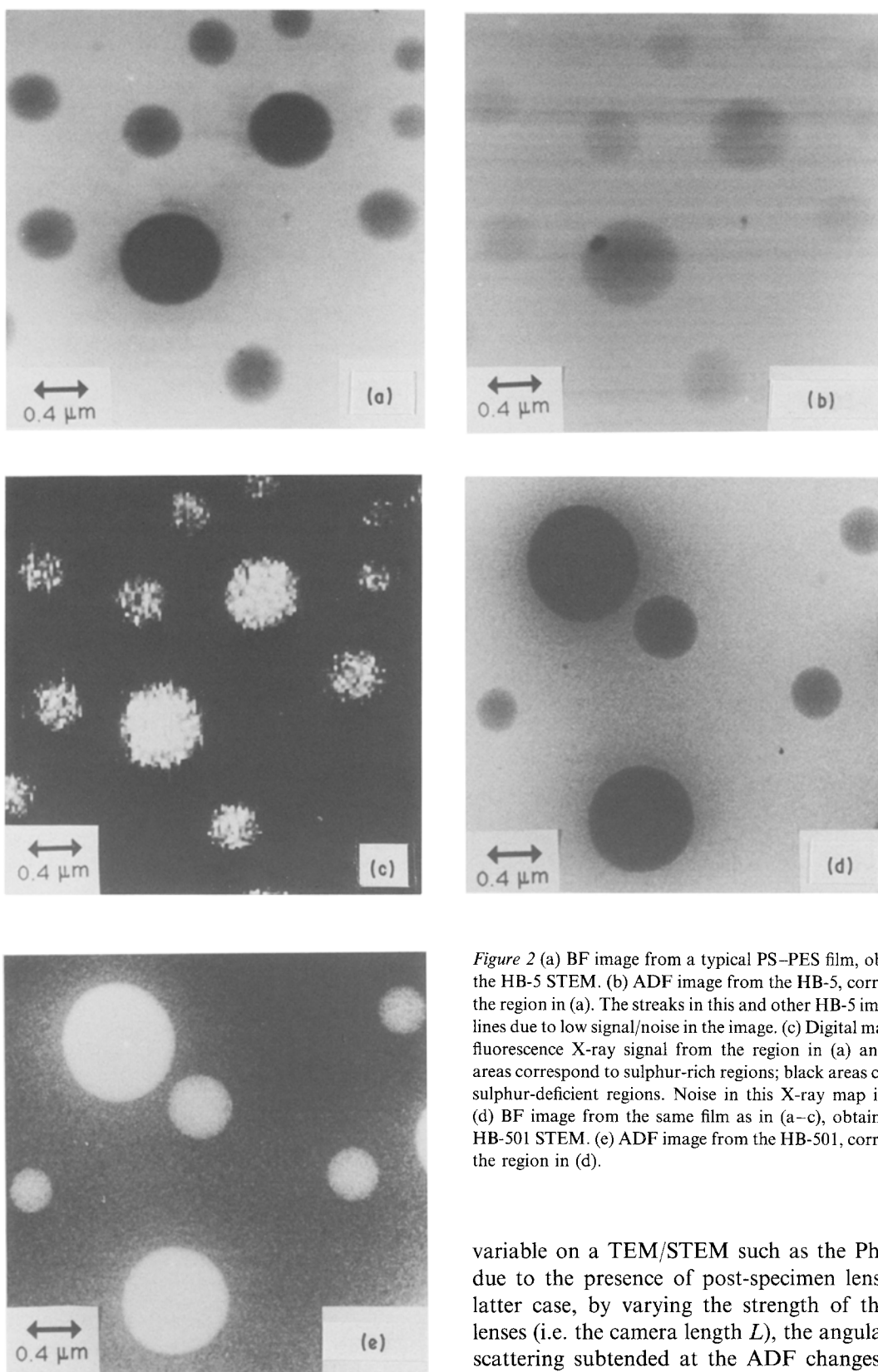


Figure 2 (a) BF image from a typical PS-PES film, obtained using the HB-5 STEM. (b) ADF image from the HB-5, corresponding to the region in (a). The streaks in this and other HB-5 images are scan lines due to low signal/noise in the image. (c) Digital map of the $SK\alpha$ fluorescence X-ray signal from the region in (a) and (b). White areas correspond to sulphur-rich regions; black areas correspond to sulphur-deficient regions. Noise in this X-ray map is shot noise. (d) BF image from the same film as in (a-c), obtained using the HB-501 STEM. (e) ADF image from the HB-501, corresponding to the region in (d).

and “mass-thickness” effects, and hence it would be difficult to interpret the image in terms of chemical composition.

3.2.1.2. *Annular dark-field detector.* This receives scattered electrons in an angular range defined by the inner and outer angles (θ_{inner} and θ_{outer}) of the detector (Fig. 1). For dedicated STEMs, such as the HB-5 and HB-501, this is a fixed angular range, whereas it is

variable on a TEM/STEM such as the Philips 400T due to the presence of post-specimen lenses. In the latter case, by varying the strength of the imaging lenses (i.e. the camera length L), the angular range of scattering subtended at the ADF changes. Table II gives details of the different angular ranges on the different microscopes.

The electrons collected by the ADF detector originate from three scattering mechanisms: coherent

TABLE II Acceptance angle ranges of ADF detectors

Microscope	θ_{inner} (mrad)	θ_{outer} (mrad)
VG HB-5	25	90
VG HB-501	50	500
Philips 400T ($L = 575$ mm)	10	70
Philips 400T ($L = 400$ mm)	20	125

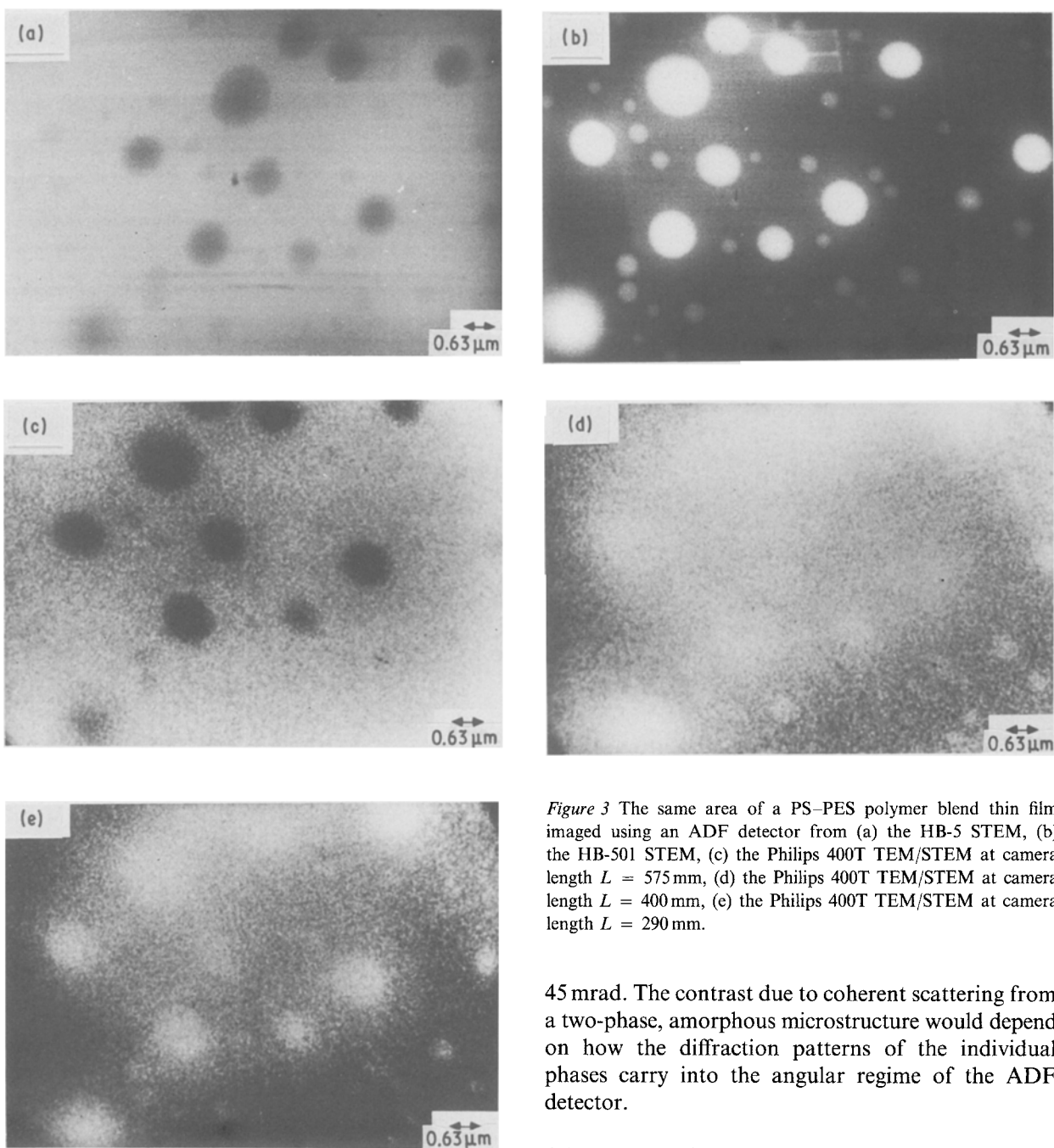


Figure 3 The same area of a PS-PES polymer blend thin film imaged using an ADF detector from (a) the HB-5 STEM, (b) the HB-501 STEM, (c) the Philips 400T TEM/STEM at camera length $L = 575$ mm, (d) the Philips 400T TEM/STEM at camera length $L = 400$ mm, (e) the Philips 400T TEM/STEM at camera length $L = 290$ mm.

elastic scattering, incoherent elastic scattering, and inelastic scattering. In thick specimens, electrons undergo multiple scattering via any or all of the above mechanisms. The probability that an incident electron will be scattered within the angular range of the detector is related to the electron scattering cross-section and thickness of the material. Each scattering mechanism has a different cross-section, with a different amplitude and angular dependence, and so each mechanism must be treated independently. Contrast between the two polymer phases in the ADF image is due to the *differences* in the electron scattering cross-section and/or thickness variations.

3.2.1.2.1. Coherent elastic scattering: thin specimens.

Coherent elastic scattering, in the case of an amorphous specimen, produces diffuse rings in the diffraction pattern. For PS-PES films, the diffraction patterns exhibit at least two distinct rings, between 15 and

45 mrad. The contrast due to coherent scattering from a two-phase, amorphous microstructure would depend on how the diffraction patterns of the individual phases carry into the angular regime of the ADF detector.

3.2.1.2.2. Incoherent elastic scattering. A uniform film of thickness t and atomic density ρ (atoms per unit volume) will give rise to an incoherent elastically scattered current, given (assuming 100% detection efficiency [9]) by

$$I_{el} = \sigma_{el} \rho t I_0 \quad (1)$$

where σ_{el} is the cross-section for incoherent elastic scattering into the annular detector, and I_0 is the incident electron current. The cross-section σ_{el} , is just the differential cross-section for elastic scattering, $d\sigma_{el}/d\Omega$, integrated over the angular range subtended by the ADF detector. The differential cross-section may be calculated using the first Born approximation (this assumes a screened Coulombic or Rutherford potential), which may be written in the following form [10]:

$$\frac{d\sigma_{el}}{d\Omega} = \left(\frac{2\gamma}{ka_H} \right)^2 \frac{Z^2}{(\theta^2 + \theta_0^2)^2} \quad (2)$$

where $\gamma = [1 - (v^2/c^2)]^{-1/2}$ in which v is the electron

velocity and c the speed of light, $k = 2\pi/\lambda$, where λ is the electron wavelength, $a_H = 0.0529$ nm is the Bohr radius, Z is the atomic number of the target atom, θ is the scattering angle, and θ_0 is the Born screening angle given [11, 12] by

$$\theta_0(\text{radians}) = \frac{1}{kr_0} = \left(\frac{1}{ka_H}\right) Z^{1/3} \quad (3)$$

In this simplified model, the screening action is approximated by a single exponential term in the Coulomb potential expression, with a Thomas–Fermi screening radius $r_0 = a_H Z^{-1/3}$ [10]. Equation 2 shows that the angular distribution of elastically scattered electrons varies as $Z^2/(\theta^2 + \theta_0^2)^2$, and since θ_0 increases with increasing Z , the intensity distribution tends to increase and broaden for scattering from heavier elements. Thus, the oxygen and sulphur constituents in PES are expected to scatter electrons more efficiently and to higher angles than the atomic species in PS (carbon and hydrogen only).

3.2.1.2.3. Inelastic scattering. The differential cross-section for inelastic scattering, $d\sigma_{\text{inel}}/d\Omega$, has a similar form to the incoherent elastic scattering (Equation 2), except that it falls off with $1/(\theta^2 + \theta_0^2)$. However, the characteristic screening angle, θ_E , which accounts for the decay of $d\sigma_{\text{inel}}/d\Omega$ with increasing θ is only ~ 0.1 mrad, compared with $\theta_0 \sim 10$ mrad, the typical order of the screening angle which accounts for the decay of $d\sigma_{\text{el}}/d\Omega$ with θ [5, 10]. Thus, inelastic scattering is much more forward-peaked than elastic scattering. Also at large scattering angles $\theta \gg \theta_0 \gg \theta_E$, incoherent elastic scattering is a factor of Z more intense than inelastic scattering [5]. For the angular regimes covered by the ADF detectors in this study (> 25 mrad), inelastic scattering is probably not important.

In summary, for uniformly thin specimens in the angular regimes of interest, the main contribution to contrast in ADF images should be from incoherent elastic scattering. Intensity due to coherent elastic scattering cannot be ignored, but it is expected that this mechanism will not produce much image *contrast*. Under conditions of uniform thickness, the ADF contrast will be primarily dependent on the average Z : regions containing atomic species of high Z will appear brighter in an ADF image than regions containing atomic species of low Z . The magnitude of the contrast depends on the average Z -differences between adjacent phases in the microstructure, and on the angular regime sampled by the ADF detector. However, because of the thickness of the specimens, the effects of multiple scattering need to be considered.

3.2.1.2.4. Multiple scattering. Multiple scattering will have the effect of convoluting all the cross-sections with themselves, an average of $(n - 1)$ times, where

$$\langle n \rangle = t/\Lambda \quad (4)$$

in which t is the film thickness and Λ is the mean free path for scattering. For thick, amorphous films, the diffraction rings will become washed out and form a

continuous decaying background over a large angular range. Little contrast will arise in thick specimens from this mechanism, even if the thicknesses of the two phases differ by a small amount. In the case of incoherent elastic scattering, the convolution of a single scattering cross-section with itself will make the resultant curve broader, and since the area under the curve must remain fixed (the total scattering probability into all angles is constant), this will lower the intensity at any given angle. The effect of multiple scattering on inelastic scattering will be the same as in the case of elastic scattering, but since $\theta_E \ll \theta_0$, beam spreading due to inelastic scattering will be much less significant than spreading due to elastic scattering. Furthermore, the inelastic intensities will be a factor of Z lower at large angles, as mentioned previously, and hence less important. Successive scattering events by two different mechanisms are also possible, e.g. an incoherent elastic event followed by an inelastic event. However, by the same reasoning as above, this will have little effect on the angular distribution and hence the contrast. Thus ADF image contrast in thick specimens should be most affected by incoherent elastic–incoherent elastic electron scattering events.

The mean free path Λ_{el} for incoherent elastic scattering, and hence the average number of scattering events per electron, $\langle n \rangle_{\text{el}}$, is different for electrons penetrating PS or PES. Λ_{el} for a multi-component polymer with η atomic species may be calculated as follows:

$$\Lambda_{\text{el}} = \left(\sum_i^{\eta} N_i \sigma_{\text{t},i}\right)^{-1} = \left(N_m \sum_i^{\eta} m_i \sigma_{\text{t},i}\right)^{-1} \quad (5)$$

where N_i is the number of atoms of the i th species per unit volume, $\sigma_{\text{t},i}$ is the total elastic scattering cross-section for the i th species, N_m is the number of monomers per unit volume, m_i is the number of atoms of the i th species per monomer, and η is the number of atomic species in the monomer. For each atomic species $\sigma_{\text{t},i}$ may be determined by combining Equations 2 and 3 and integrating over all solid angles (noting that the small-angle approximation is valid here, i.e. $\sin \theta \simeq \theta$):

$$\sigma_{\text{t},i} = \int_0^{\infty} 2\pi\theta \left(\frac{d\sigma_{\text{el}}}{d\Omega}\right)_i d\theta = \frac{1}{\pi} \left(\frac{\lambda_C^2}{\beta^2}\right) Z_i^{4/3} \quad (6)$$

where $\lambda_C = 0.002426$ nm is the Compton wavelength of an electron, Z_i is the atomic number of the i th species, and $\beta = v/c$.

The values for $\sigma_{\text{t},i}$ for the constituents of PS and PES together with the resultant values for the polymers are listed in Table III. Considering the film thicknesses of the polymer film used in this study (~ 410 nm as measured with a stylus profilometer), it is clear from the calculated values for $\Lambda_{\text{el}}(\text{PS})$ and $\Lambda_{\text{el}}(\text{PES})$ that multiple scattering is important in these films. Furthermore, the average number of scattering events per unit distance penetrated is different for PS and PES. Comparing $\Lambda_{\text{el}}(\text{PS})$ and $\Lambda_{\text{el}}(\text{PES})$ in Table III, it is evident that 100 keV electrons travel $\sim 30\%$ further (on average) in PS than in PES, before undergoing a scattering event. Equivalently, an electron under-

TABLE III Calculated screened Rutherford cross-sections and mean free paths for incoherent elastic scattering of 100 keV electrons, and related data

Species	Z	θ_0 (mrad)	σ_t (nm ²)	m		$\Lambda_{el,i}$ (nm)	
				(PS)	(PES)	PS*	PES†
H	1	11.13	6.235×10^{-6}	8	8	3288	5633
C	6	20.23	6.798×10^{-5}	8	12	301.5	344.4
O	8	22.26	9.976×10^{-5}		3		938.8
S	16	28.05	2.514×10^{-4}		1		1118
PS			5.937×10^{-4}			276.2 = $\Lambda_{el}(PS)$	
PES			1.416×10^{-3}			198.4 = $\Lambda_{el}(PES)$	

* Using $N_{PS} = 6.098$ monomers per nm³.

† Using $N_{PES} = 3.559$ monomers per nm³.

goes 30% more scattering events in PES than in PS, for equal-thickness polymers. Thus, the multiply convoluted curves which account for plural scattering are lowered and spread out more in the case of PES than in PS. This may cause the scattering curves to overlap, such that within some angular range PS may scatter more intensity into an ADF detector than PES. Such a result cannot be obtained by considering the single-scattering cross-sections only.

3.3. Comparison of theory and experiment:

PS–PES electron images

If one is to achieve any quantitative appreciation of the ADF image observations presented earlier, it is necessary to measure the microstructure contrast

quantitatively, and to calculate the scattered intensity profiles $I(\theta)$ of a microstructural feature, such as an inclusion and the surrounding matrix as observed in Figs 2 and 3. It would also be beneficial if one could determine how the ADF intensity ratio $I_{inclusion}/I_{matrix}$, relates to the composition ratio of such adjacent features. To determine $I_{inclusion}(\theta)$ and $I_{matrix}(\theta)$, one must account for multiple incoherent elastic–incoherent elastic scattering events as discussed above.

In Figs 4a and b the contrast observed in an ADF image from the same specimen as in Figs 2 and 3 is quantified (in the case of the HB-501). Using the ADF intensity trace in Fig. 4b, an intensity ratio $I_{inclusion}/I_{matrix}$ was determined, relative to the baseline provided by the intensity from the nearby hole in the film. It was

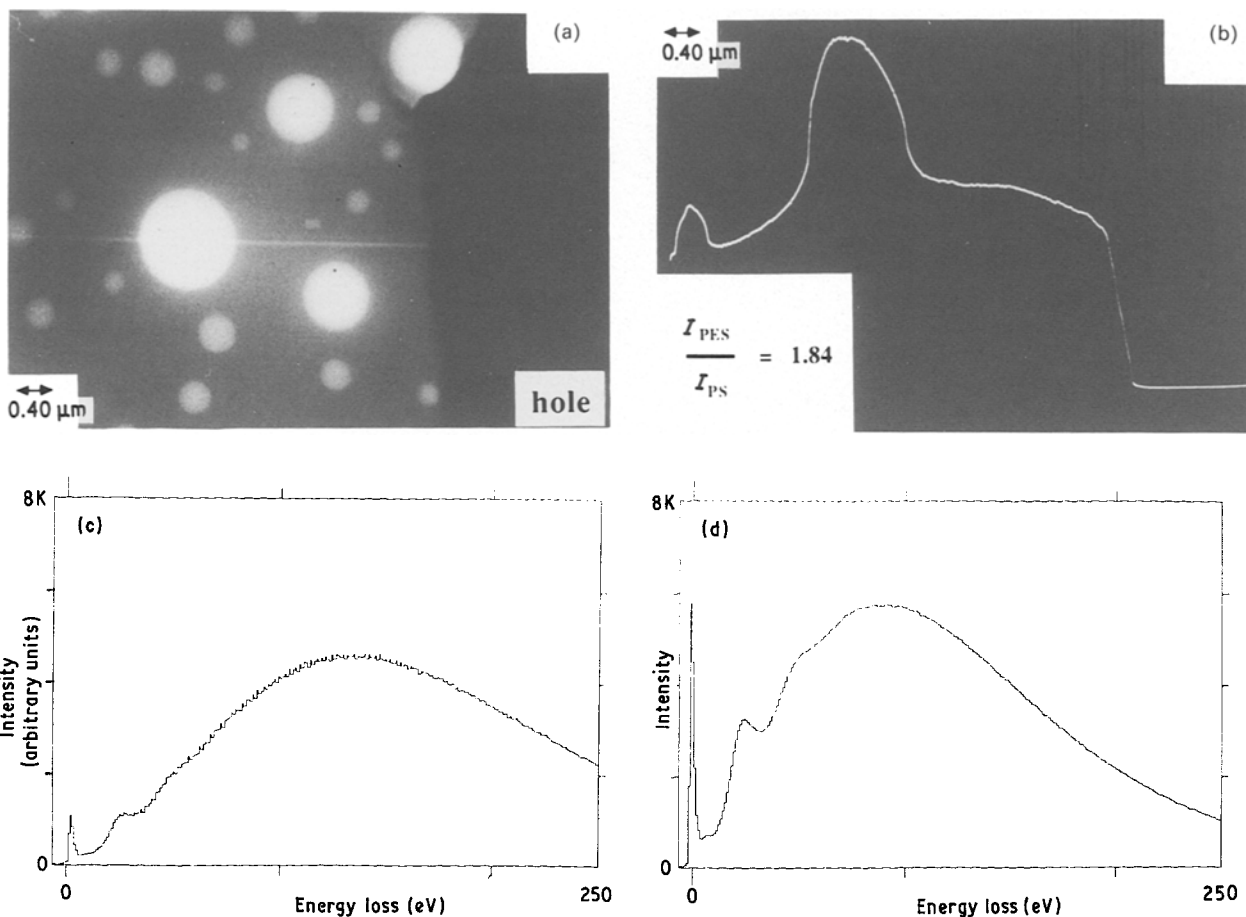


Figure 4 (a) ADF image from the edge of the PS–PES thin film obtained using the HB-501 STEM. (b) ADF line trace of the intensity along a line through the large inclusion, the matrix and the hole in the foil (white line in (a) shows position of line trace). (c) EELS spectrum from the centre of the large inclusion ($t \sim 0.51 \mu\text{m}$). (d) EELS spectrum from the matrix material near the large inclusion ($t \sim 0.28 \mu\text{m}$).

found that the intensity at the centre of the large PES-rich inclusion compared with the intensity at the nearby PS-rich matrix had a ratio $I_{\text{inclusion}}/I_{\text{matrix}} = 1.7$.

Figs 4c and d show EELS spectra taken from the centre of the large inclusion in Fig. 4a and the surrounding matrix, respectively. From these spectra it was determined that the thickness of the PES-rich inclusion was $t_{\text{PES}} \sim 510$ nm, whereas the thickness of the surrounding PS-rich matrix was only $t_{\text{PS}} \sim 280$ nm. (These values are to be compared with the stylus profilometer measurement of ~ 410 nm, which can be regarded as an average for the two phases.) This result implies that the largest PES-rich inclusions actually stand proud of the film. Both of these thicknesses are greater than or equal to the calculated mean free paths from Table III for 100 keV elastically scattered electrons in PES and PS ($\Lambda_{\text{el}}(\text{PS}) \sim 200$ nm and $\Lambda_{\text{el}}(\text{PES}) \sim 280$ nm). This confirms the necessity of considering multiple scattering for a quantitative understanding of the observed intensity ratio.

Crewe and Groves [12] outline a method of approach to multiple scattering calculations in thick specimens, when inelastic and elastic scattering must be taken together to account for BF image contrast. Their method can be adapted to the ADF image situation here, because even though only elastic–elastic events are believed to be important for the contrast, the scattering may arise from distinct atomic species, since these are multiple-component materials. This is analogous to considering scattering from more than one mechanism.

For electrons traversing a thickness t of a multiple-component material it is necessary to find the angular distribution $F(t, \theta)$ of electrons that have travelled through $n_1 = t/\lambda_1$ elastic mean free paths with respect to atomic Species 1, $n_2 = t/\lambda_2$ elastic mean free paths with respect to Species 2, etc. As an example, for a four-component material like PES, following the outline of Crewe and Groves,

$$I(t, \theta) \propto \sum_{j=0}^{\infty} \sum_{k=0}^{\infty} \sum_{l=0}^{\infty} \sum_{m=0}^{\infty} P_{j,k,l,m}(t) F_{j,k,l,m}(\theta) \quad (7)$$

where j, k, l and m label the number of elastic scattering events from atomic Species 1, 2, 3 and 4, respectively. The quantity $P_{j,k,l,m}(t)$ is the probability that an electron will scatter exactly j times from Species 1, k times from Species 2, l times from Species 3 and m times from Species 4 in traversing the thickness t . Since electron scattering obeys Poisson statistics (e.g. [5]), this probability is the product of four Poisson factors:

$$P_{j,k,l,m}(t) = \left(\frac{n_1^j}{j!} \exp(-n_1) \right) \left(\frac{n_2^k}{k!} \exp(-n_2) \right) \times \left(\frac{n_3^l}{l!} \exp(-n_3) \right) \left(\frac{n_4^m}{m!} \exp(-n_4) \right) \quad (8)$$

The other quantity in Equation 7, $F_{j,k,l,m}(\theta)$, is obtained via multiple convolution of the differential cross-section curves for single elastic scattering. If one denotes the differential cross-sections for incoherent elastic scattering (Equation 2) from atomic Species 1, 2, 3 and 4 by $d\sigma/d\Omega_1(\theta)$, $d\sigma/d\Omega_2(\theta)$, $d\sigma/d\Omega_3(\theta)$ and

$d\sigma/d\Omega_4(\theta)$, respectively, and normalizing the $d\sigma/d\Omega_i(\theta)$ such that

$$\int_0^{\infty} 2\pi\theta \left(\frac{d\sigma}{d\Omega_i(\theta)} \right) d\theta = 1$$

then

$$F_{j,k,l,m}(\theta) = (d\sigma/d\Omega_1)**(d\sigma/d\Omega_1)** \dots (d\sigma/d\Omega_1)**(d\sigma/d\Omega_2)** \dots ** (d\sigma/d\Omega_4)**(d\sigma/d\Omega_4) \quad (9)$$

where $**$ represents a two-dimensional convolution; $d\sigma/d\Omega_1$ appears j times, $d\sigma/d\Omega_2$ appears k times, $d\sigma/d\Omega_3$ appears l times and $d\sigma/d\Omega_4$ appears m times (the order of the factors is independent of the order in which the scattering events may occur).

A reasonable approximation to the rigorous but difficult computation represented by Equations 7 to 9 may be obtained by lumping the mean free paths Λ_1 , Λ_2 etc. together to produce a single mean free path for scattering from a particular structural unit of material. In the case of a polymer, this is most easily done by considering a monomer unit, and then the mean free path of interest is equivalent to either $\Lambda_{\text{el}}(\text{PS})$ or $\Lambda_{\text{el}}(\text{PES})$, as determined from Equation 5 and given in Table III. In this approximation, one imagines the scattering to occur from an ‘‘average atom’’, whose scattering cross-section curve is a weighted average of the differential cross-sections of the atomic species that make up the monomer, with a weighting according to the abundance of the species in the monomer, i.e.

$$\left(\frac{d\sigma_{\text{el}}}{d\Omega} \right)_{\text{monomer}} = \sum_i^{\eta} m_i \left(\frac{d\sigma_{\text{el}}}{d\Omega} \right)_i \quad (10)$$

where η and m_i are as defined in Equation 5 and $(d\sigma_{\text{el}}/d\Omega)_i$ is the elastic differential cross-section curve for the i th atomic species, as given by Equations 2 and 3. Such curves for the monomers of PS and PES, as calculated from Equations 2, 3 and 10, are illustrated in Fig. 5a.

From Equation 1, the scattered intensity ratio $I_{\text{PS}}/I_{\text{PES}}$ for equivalent thicknesses of PS and PES is proportional to $Q_{\text{PS}}/Q_{\text{PES}}$ (where Q_{PS} and Q_{PES} represent monomer densities for PS and PES, respectively). Then, assuming that we have a very small acceptance angle for the ADF detector, such that $\sigma_{\text{el}}(\theta)$ in Equation 1 is approximately equal to $d\sigma_{\text{el}}(\theta)/d\Omega$, it is possible to calculate a comparison of $I_{\text{PS}}(\theta)$ with $I_{\text{PES}}(\theta)$ by simply multiplying the $d\sigma_{\text{el}}(\theta)/d\Omega$ for PS in Fig. 5a by a factor $Q_{\text{PS}}/Q_{\text{PES}}$. Fig. 5b illustrates the use of the monomer scattering curves to determine the angular distribution of electron intensity in this way. However, the intensity curves in Fig. 5b are only valid in the limit of very thin films, wherein multiple scattering effects may be ignored. Fig. 5b illustrates the fact that ADF contrast reversal is not explicable in the limit of single scattering: in this thin-film limit, PES should appear brighter than PS over all ADF angular regimes. Thus, in the light of the observations for the PS–PES films discussed here, and given the calculated mean free paths, it is necessary to take into account multiple scattering in the intensity distribution calculations.

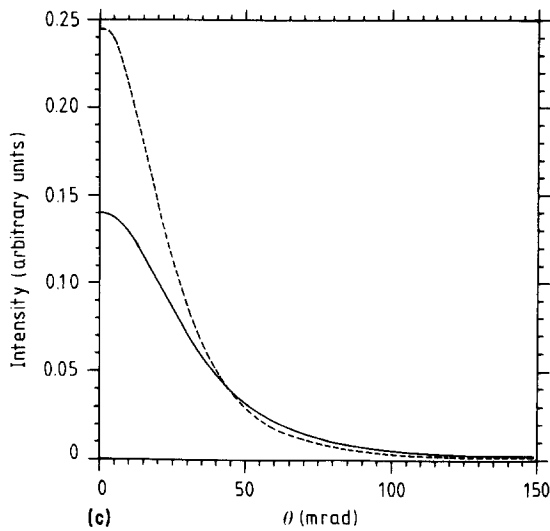
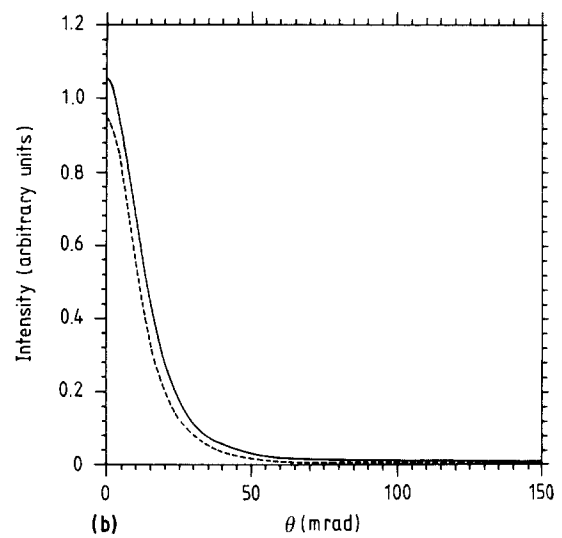
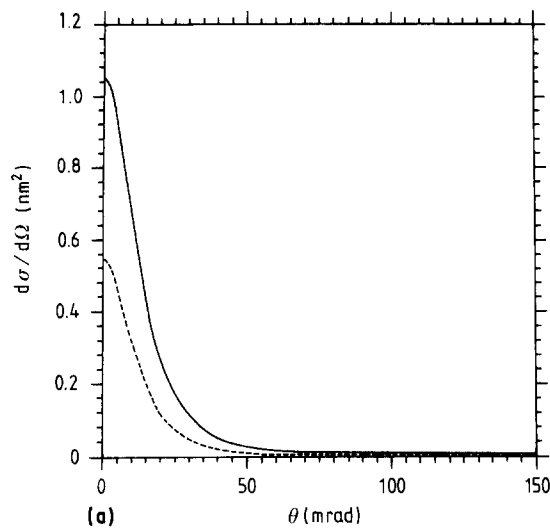


Figure 5 (a) Differential cross-section, $d\sigma/d\Omega$, for incoherent elastic scattering against scattering angle, θ , for scattering from a (—) pure PES or (---) pure PS monomer (arbitrary units). See text for a discussion of all calculations. (b) Detected intensity, I , for incoherent elastic scattering, against θ , for scattering from a thin film of (—) pure PES or (---) pure PS, where single scattering is valid (arbitrary units). (c) Detected intensity, I , for incoherent elastic scattering, against θ , for scattering from a thick film of (—) pure PES or (---) pure PS, where multiple scattering must be considered (arbitrary units). For this example, the thicknesses assumed for the PES and PS were 510 and 280 nm, respectively. This example represents the conditions present in the case of the PES-rich inclusion and the surrounding PS matrix in Fig. 4.

Using the “average atom” curve described by Equation 10, the calculation outlined in Equations 7 to 9 is greatly simplified, such that the intensity distribution for scattering from a polymer film of thickness t is approximated by a single sum of multiple-scattering functions with Poisson weighting coefficients

$$I(t, \theta) \propto \sum_{n=0}^{\infty} \left[\frac{1}{n!} \left(\frac{t}{\Lambda_{el}} \right)^n \exp \left(-\frac{t}{\Lambda_{el}} \right) \right] F_n(\theta) \quad (11)$$

where n is the number of elastic scattering events from each “average atom” (i.e. monomer), Λ_{el} is the mean free path given by Equation 5, and the $F_n(\theta)$ are multiple scattering functions determined from $(n - 1)$ -fold convolutions:

$$F_n(\theta) = F_{n-1}(\theta) ** F_1(\theta) \quad (12)$$

$F_1(\theta)$ is simply $(d\sigma_{el}/d\Omega)_{\text{monomer}}$ normalized over solid angle to equal unity, similar to the $d\sigma/d\Omega_i(\theta)$ in Equation 9.

Fig. 5c shows the results of a multiple scattering calculation employing Equations 11 and 12 for PES and PS, assuming $t_{\text{PES}} = 510$ nm and $t_{\text{PS}} = 280$ nm, the values obtained for the PES inclusion and PS matrix in Fig. 4 from EELS. The two-dimensional convolutions required in this calculation were performed by using projected distributions to reduce each convolution to a one-dimensional integration. This

procedure is described in detail by Misell and Burge [13]. The results clearly demonstrate the crossover of the PES and PS intensity distributions, a necessary result to explain the contrast reversal observed using the various ADF detector arrangements described earlier.

Table IV shows the contrast reversal expected for the Philips 400T ADF detector (operating at camera lengths $L = 575$ and 400 mm), and for the HB-501 ADF detector, as determined from the intensity curves for PES and PS in Fig. 5c and using the following definitions of contrast:

$$\text{ADF contrast} \equiv \frac{\int_{\theta_{\text{inner}}}^{\theta_{\text{outer}}} I_{\text{PES}}(t_{\text{PES}}, \theta) d\theta}{\int_{\theta_{\text{inner}}}^{\theta_{\text{outer}}} I_{\text{PS}}(t_{\text{PS}}, \theta) d\theta} \quad (13)$$

The calculations were performed for 100 keV electrons, so a comparison of the calculations with the HB-5 observations is not valid. The calculations verify that dark-contrast PES spheres are expected in the low-angular range condition, i.e. for the Philips ADF detector at $L = 575$ mm, as was observed (Fig. 3c). However, for the intermediate angular range of the Philips ADF detector at $L = 400$ mm, the experimentally observed intensity crossover (Fig. 3d) is not quite predicted (although almost). For the high-angle range appropriate to the HB-501 detector, the calculations do predict bright-contrast PES spheres, as observed (Figs 2e, 3b and 4a) and in agreement with Z-contrast expectations. However, quantitative agreement is not obtained. The experimentally measured

TABLE IV Calculated PES/PS ADF contrast for 100 keV electrons

Material	t (nm)	Λ_{cl} (nm)	τ/Λ_{cl}	ADF detector	θ_{inner} (mrad)	θ_{outer} (mrad)	Contrast, I_{PES}/I_{PS}
PES	510	198.4	2.571	Philips 400T ($L = 575$ mm)	10	70	0.782
PS	280	276.2	1.014	Philips 400T ($L = 400$ mm)	20	125	0.932
				VG HB-501	50	500	1.347
PES	561	198.4	2.828	Philips 400T ($L = 575$ mm)	10	70	0.752
PS	252	276.2	0.912	Philips 400T ($L = 400$ mm)	20	125	0.920
				VG HB-501	50	500	1.400

ADF contrast from the HB-501 (Fig. 4b) is 1.7, while the calculated contrast for this configuration is only 1.35 (Table IV). Table IV also indicates the results of a calculation in which the thicknesses of the PES and PS were altered by 10% each, and in the opposite sense, since it is possible that the EELs thickness measurements are at least 20% in error. But Table IV shows that the calculations seem to be rather insensitive to such thickness variations, at least for these “thick” films. In any case, quantitative agreement is still not obtained in this way.

The discrepancies between the experiments and the calculations described above are probably a result of the approximations involved. First, Langmore *et al.* [14] warn against the use of the Lenz–Wentzel model due to the inaccuracies of the model compared with cross-sections derived from other theories (more accurate potentials are reviewed by Scott [15]). However, the Lenz–Wentzel inaccuracies tend to be most pronounced for heavy atoms [14], so it was not anticipated that the model would present difficulties for the low Z species present in these polymers. Secondly, the use of an “average atom” model to account for multiple scattering is an oversimplification of the actual physical processes. In future calculations it would be desirable to carry out a more rigorous numerical treatment. It may also prove prudent to include *elastic* and *coherent* scattering in the multiple scattering treatment. The calculations presented here, however, do portray qualitatively the features observed in experiments. At this stage, the calculations are not accurate enough to derive compositional information from ADF imaging experiments. If improved, however, the image analysis procedures described here may prove particularly useful for analysing situations where component mixing is present, i.e. in the case of partially miscible blends. Such component mixing has been observed by the authors in the present system [16], although it is believed not to be an equilibrium effect.

4. Conclusions

This study has demonstrated some possible procedures for performing microanalysis on polymer blend thin films using a STEM. It has also demonstrated the complexities involved when thin films specimens are

not “thin” and do not possess uniform thickness. Using the $SK\alpha$ fluorescence X-ray signal for EDS analysis, it is possible to obtain compositional information on neighbouring microstructural phases in PS–PES polymer blend thin films. The films examined here are seen to consist of spherical inclusions that are PES-rich compared with the matrix.

However, to obtain chemical information directly from ADF images to date remains an unattained goal. Naïve interpretation of the images can be most misleading, since the contrast between phases can vary drastically according to the effective geometry of the detector. Arguments have been presented to show that the ADF images are consistent with the EDS data, when considered in detail, but image interpretation is extremely complicated. Nevertheless it is well worth continuing to try to quantify these images (as has been done for crystalline materials [4]), since the information is obtained much faster than in spectroscopic experiments such as EDS. This is of particular advantage in the study of beam-sensitive materials.

Acknowledgements

The authors would like to thank Dr L. M. Brown for useful conversations, Dr W. M. Stobbs for the use of his Philips 400T STEM instrument in the Department of Metallurgy, University of Cambridge, Dr A. E. Dray of Philips-U.K. for advice and assistance, and the SERC for supporting one of us (K.E.S.).

References

1. B. D. LAUTERWASSER and E. J. KRAMER, *Phil. Mag.* **39a** (1979) 469.
2. R. A. L. JONES, J. KLEIN and A. M. DONALD, *Nature* **321** (1986) 161.
3. M. A. PARKER and D. VESELY, *J. Polym. Sci. Polym. Phys.* **24** (1986) 1869.
4. S. J. PENNYCOOK, S. D. BERGER and R. J. CULBERTSON, *J. Microsc.* **144** (1986) 229.
5. L. REIMER, “Transmission Electron Microscopy: Physics of Image Formation and Microanalysis” (Springer, Berlin, 1984).
6. R. F. EGERTON, *Phil. Mag.* **31** (1975) 199.
7. R. A. FERREL, *Phys. Rev.* **101**, (1956) 554.
8. L. M. BROWN, *J. Phys. F* **11** (1981) 1.
9. A. V. CREWE, J. P. LANGMORE and M. S. ISAACSON, in “Physical Aspects of Electron Microscopy and Microbeam Analysis”, edited by B. M. Siegel and D. R. Beaman (Wiley, New York, 1975) p. 53.

10. F. LENZ, *Z. Naturforsch.* **A9** (1954) 185.
11. G. WENTZEL, *Z. Phys.* **40** (1927) 590.
12. A. V. CREWE and T. GROVES, *J. Appl. Phys.* **45** (1974) 3662.
13. D. L. MISELL and R. E. BURGE, *J. Phys. C.* **2** (1969) 61.
14. J. P. LANGMORE, J. WALL and M. S. ISAACSON, *Optik* **38** (1973) 335.
15. W. T. SCOTT, *Rev. Mod. Phys.* **35** (1963) 231.
16. K. E. SICKAFUS and A. M. DONALD, to be submitted.

*Received 28 May
and accepted 24 July 1987*